Supporting Information: Convective Environments Over the Arabian Peninsula in Current and Future Climates: A Machine Learning Approach

Ahmed Homoudi[1], Henning W. Rust[2], Klemens Barfus[3], Christian Bernhofer[1], and Matthias Mauder[1]

[1]Institute of Hydrology and Meteorology, TUD Dresden University of Technology, Pienner Strasse 23, 01737 Tharandt, Germany

[2]Institute of Meteorology, Freie Universität Berlin, Carl-Heinrich-Becker-Weg 6-10, 12165 Berlin, Germany

[3]Independent Researcher, Dresden, Germany

Correspondence: Ahmed Homoudi (ahmed.homoudi@tu-dresden.de)

1 TEXT S1: Regional warming and anomalies estimation

The regional warming was estimated first from each dataset and then averaged to yield +1.22 °C. From each dataset, we estimate the area-weighted monthly anomalies over the AP, then the resulting time series was averaged to annual means, which are subsequently averaged over the period 2001-2024. The regional warming values for the period 2001 - 2024 relative to the preindustrial level (1850 - 1900) based on the area-weighted average are +1.216 °C, +1.265 °C, +1.082 °C, and +1.290 °C for Berkeley Earth, NOAA Global Temp, HadCRUT5, and GISTEMP, respectively.

For each grid cell (i, j), the monthly-diurnal climatology is estimated by pooling all values across years for a given month m and hour h:

$$\bar{X}_{i,j,m,h} = \frac{1}{N}\sum_{n=1}^{N} X_{i,j,n,m,h}\,, \tag{1}$$

The anomaly at grid cell (i, j) for variable X at time t is then:

$$X'_{i,j,t} = X_{i,j,t} - \bar{X}_{i,j,m(t),h(t)} \tag{2}$$

where $m(t)$ and $h(t)$ denote the month and hour corresponding to time t, and N is the total number of samples for month m and hour h across all years. Noteworthy, indices with strictly positive or bounded ranges or spatiotemporal covariates were used in their original absolute form.

2 TEXT S2: Calibration metrics

The conditional probability of a CE given the feature vector ξ is $f(\xi) = P(y = 1 \mid \xi)$. The Brier Score (BS) is given by:

$$BS = \frac{1}{N}\sum_{i=1}^{N}(f(\xi_i) - y_i)^2 \tag{3}$$

where N is the number of samples, $f(\xi_i) \in [0,1]$ is the model's predicted probability, and $y_i \in \{0,1\}$ is the observed binary label. The Brier Skill Score (BSS) is given by:

$$BSS = 1 - \frac{BS}{BS_{ref}} \tag{4}$$

where BS_{ref} is the BS of a reference forecast or the climatological probability of CEs (g). Murphy (1973) derived an algebraic decomposition of the BS estimated from the binned predicted probabilities as:

$$BS = \underbrace{\frac{1}{N}\sum_{k=1}^{K} n_k\left(f_k - \bar{o}_k\right)^2}_{\text{REL}_k} - \underbrace{\frac{1}{N}\sum_{k=1}^{K} n_k\left(\bar{o}_k - g\right)^2}_{\text{RES}_k} + \underbrace{g(1-g)}_{\text{UNC}} \tag{5}$$

where K is the number of bins, REL_k and RES_k are the bin's reliability and resolution, respectively. UNC is the uncertainty that depends mainly on the climatological frequency of CEs. Here, n_k represents the number of samples in bin k, f_k denotes the mean predicted probability of CEs within the bin, and $\bar{o}_k = \frac{1}{n_k}\sum_{i \in k} y_i$ indicates the observed frequency of CEs in the bin.

The Expected Calibration Error (ECE; Naeini et al., 2015) is given by:

$$\text{ECE} = \sum_{k=1}^{K} \frac{n_k}{N}\left|f_k - \bar{o}_k\right| \tag{6}$$

3 Text S3: Binary label definition

To define the label from IMERG data for CEs in the ERA5 dataset, we tested multiple percentiles of the areal-averaged 6h precipitation, ranging from the 50$^{\text{th}}$ to the 99$^{\text{th}}$ percentile. The 50$^{\text{th}}$ percentile or the median indicates that these atmospheric profiles can produce above-median events, and the 99th percentile indicates extreme events. Additionally, the 6 h precipitation was estimated considering accumulation centred within the 6h windows or at the beginning of each window. The combination of 7 percentiles and 2 accumulations results in 14 label variations. We followed a data-driven approach and used the label's definition that showed the highest AUCPR. The three ML models were trained using the default hyperparameters and evaluated using AUCPR, FAR, HSS, and POD. Illustrated in Fig. S1 is the performance of the ML models for the 14 label definitions. It is clear that all ML models achieve their best performance at the 50$^{\text{th}}$ percentile, with precipitation accumulated at the middle of the time window. In addition, performance degrades rapidly in RF and DL with increasing percentile. However, XGB does not show a similar pattern.

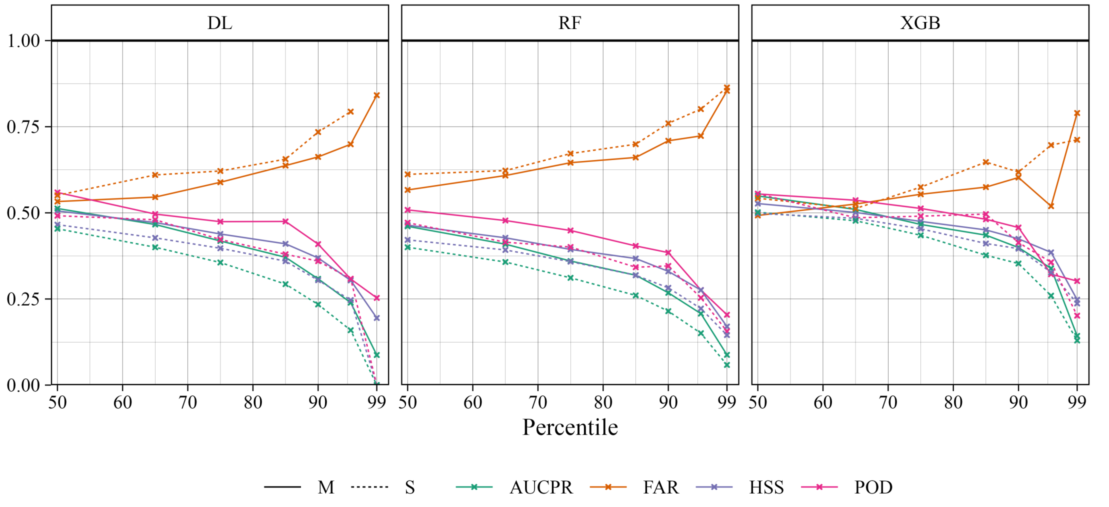

Figure S1. Performance metrics of DL, RF, and XGB across 14 label variations for CEs. Considering precipitation accumulation at the middle (M) or the start (S) of the time window.

4 Text S4: Sensitivity analysis (sampling ratio)

A highly imbalanced dataset poses a challenge for ML learning models, as there are few examples of the positive class for them to learn from. Thus, oversampling the positive events is necessary, especially in tree-based ML models. We examined the RF and XGB performance as a function of the oversampling ratio and chose the one that yielded the highest AUCPR. The ML models were trained using the default hyperparameters. We undersampled 50% of the non-CEs and then oversampled the CEs, e.g., 15% of the size of the undersampled data, resulting in 13% prevalence of positive cases in the training set. The 50% undersampling ratio was chosen to reduce the models' training time and memory usage. Figure S2 shows the performance metrics for different sampling ratios ranging from 15% to 95%. The optimal fraction of CEs for RF and XGB was determined to be 15%. based on the AUCPR. RF performance metrics degrade as the prevalence of CEs increases, whereas XGB shows relatively stable performance.

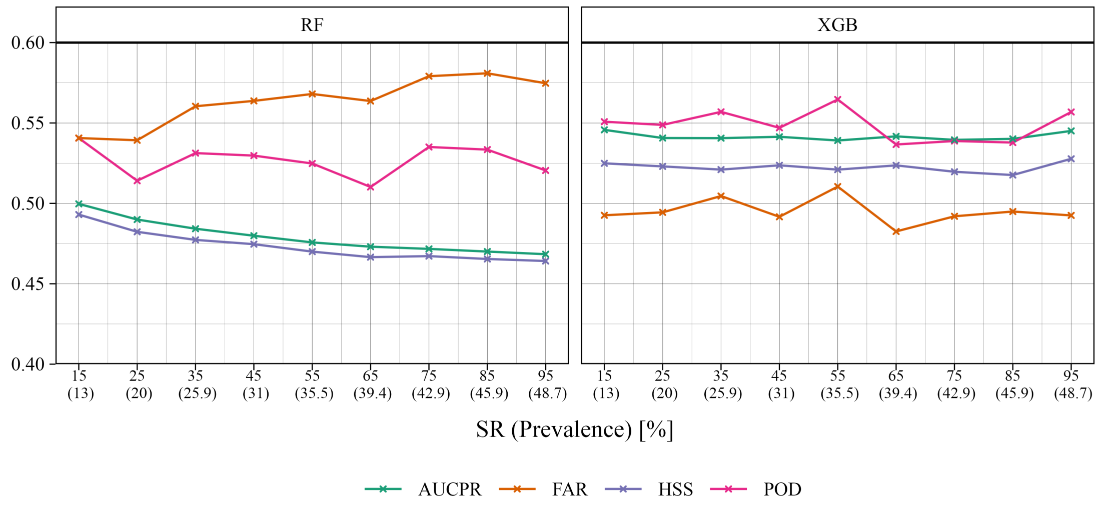

Figure S2. Performance metrics of RF and XGB across different prevalence of CEs in the training dataset.

Table S1: List of convective indices used in the study. [a] indicates that these predictors were used in their absolute form.

Begin of Table			
No.	Variable	Definition	Units
001	LL_u	eastward component of the 1000–850 hPa layer-mean wind.	m s^{-1}
002	LL_v	northward component of the 1000–850 hPa layer-mean wind.	m s^{-1}
003	LL_div	horizontal divergence of the 1000–850 hPa layer-mean wind.	s^{-1}
004	LL_rv	relative vorticity of the 1000–850 hPa layer-mean wind.	s^{-1}
005	ML_u	eastward component of the 700–400 hPa layer-mean wind.	m s^{-1}
006	ML_v	northward component of the 700–400 hPa layer-mean wind.	m s^{-1}
007	ML_div	horizontal divergence of the 700–400 hPa layer-mean wind.	s^{-1}
008	ML_rv	relative vorticity of the 700–400 hPa layer-mean wind.	s^{-1}
009	UL_u	eastward component of the 300–150 hPa layer-mean wind.	m s^{-1}
010	UL_v	northward component of the 300–150 hPa layer-mean wind.	m s^{-1}
011	UL_div	horizontal divergence of the 300–150 hPa layer-mean wind.	s^{-1}
012	UL_rv	relative vorticity of the 300–150 hPa layer-mean wind.	s^{-1}
013	VIMF_x	vertically integrated eastward moisture flux from 1000 to 300 hPa.	kg m^{-1} s^{-1}
014	VIMF_y	vertically integrated northward moisture flux from 1000 to 300 hPa.	kg m^{-1} s^{-1}
015	VIMFC	vertically integrated moisture convergence from 1000 to 300 hPa.	kg m^{-2} s^{-1}
016	thetaE850	equivalent potential temperature at 850 hPa.	K

Continuation of Table S1			
No.	Variable	Definition	Units
017	thetaE850_advec	advection of thetaE850.	K m^{-1}
018	thetaE850_grad	gradient of thetaE850.	K s^{-1}
019	thetaE_sfc	equivalent potential temperature near surface (2 m)	K
020	thetaE_sfc_advec	advection of thetaE_sfc.	K m^{-1}
021	thetaE_sfc_grad	gradient of thetaE_sfc	K s^{-1}
022	UL_EPV	mean Ertel potential vorticity between 300 and 150 hPa.	m^{2} s^{-1} K kg^{-1}
023	Max_EPV_n7	maximum of the UL_EPV within a 7×7 grid window	m^{2} s^{-1} K kg^{-1}
024 .. 033	zg_i	geopotential on pressure levels 1000–100 hPa with 100 hPa step.	m^{2} s^{-2}
034	divQvect300	divergence of Q-vectors at 300 hPa.	m kg^{-1} s^{-1}
035	divQvect500	divergence of Q-vectors at 500 hPa.	
036	divQvect700	divergence of Q-vectors at 700 hPa.	
037	divQvect850	divergence of Q-vectors at 850 hPa.	
038	omega500	vertical velocity (pressure) at 500 hPa.	Pa s^{-1}
039	omega850	vertical velocity (pressure) at 850 hPa.	
040	orog_flow	orographic upslope flow for 0-1500 m layer above ground level.	m s^{-1}
041	ML_orog_flow5	maximum of the orog_flow within a 5×5 grid window.	
042	WSh0_1_mag	wind shear 0-1 km above ground.	m s^{-1}
043	WSh0_3_mag	wind shear 0-3 km above ground.	
044	WSh0_6_mag	wind shear 0-6 km above ground.	
045 046	WSh0_1_dir	wind shear direction 0-1 km above ground, represented using cyclic components: *WSh0_1_dirc* and *WSh0_1_dirs*	-
047 048	WSh0_3_dir	wind shear direction 0-1 km above ground, represented using cyclic components: *WSh0_3_dirc* and *WSh0_3_dirs*	-
049 050	WSh0_6_dir	wind shear direction 0-1 km above ground, represented using cyclic components: *WSh0_6_dirc* and *WSh0_6_dirs*	-
051	PW	precipitable water vapour accumulated from 1000 to 100 hPa.	mm
052	td2m	dew-point temperature near surface (2 m)	K
053	ta2m	air temperature near surface (2 m)	K
054	HumI	humidity index = $(ta_{850} - td_{850}) + (ta_{700} - td_{700}) + (ta_{500} - td_{500})$	K
055	KI	K index = $(ta_{850} - ta_{5000}) + td_{850} - (ta_{700} - td_{700})$	K

Continuation of Table S1			
No.	Variable	Definition	Units
056	SHOW	Showalter index = $ta_{500} - ta'_{850\text{ hPa}\to 500\text{ hPa}}$	K
057[a] .. 066[a]	hur_i	relative humidity on pressure levels 1000–100 hPa with 100 hPa step.	%
067[a]	mu_CAPE_HVD	Convective Available Potential Energy (CAPE) of the most unstable parcel, defined as the parcel with the highest equivalent potential temperature within the lowest 300 hPa above the surface, following Haklander and Van Delden (2003).	J kg^{-1}
068[a]	mu_pLCL_HVD	pressure of the lifting condensation level (LCL) for the most unstable parcel, defined in 067.	hPa
069[a]	ml100_CAPE	CAPE for a mixed-layer parcel constructed from the ln p-weighted mean temperature, dew-point temperature, and pressure of the 100 hPa layer immediately above the surface, following Haklander and Van Delden (2003).	J kg^{-1}
070	ml100_pLCL	pressure of the LCL for the 100 hPa mixed-layer parcel, defined in 069.	hPa
071[a]	sfc_CAPE	CAPE for a parcel with the temperature, dew-point temperature and pressure near the surface (2 m) .	J kg^{-1}
072	sfc_pLCL	pressure of the LCL for the surface parcel, defined in 071.	hPa
073	LI_100ml	Lifted Index (LI) for a 100 hPa mixed-layer parcel, defined in 069, lifted pseudo-adiabatically to 500 hPa. $LI_{100ml} = ta_{500} - ta'_{100ml\to 500\text{ hPa}}$	K
074	LI_mu	LI for the most unstable parcel, defined in 067, lifted pseudo-adiabatically to 500 hPa. $LI_{mu} = ta_{500} - ta'_{mu\to 500\text{ hPa}}$	K
075	WBZH	height at which the wet-bulb temperature reaches 0 °C	m
076	SI	S index as defined by Reymann et al. (1998).	-
077	LL_LR	lapse rate of air temperature between the near surface (2 m) and 850 hPa.	K km^{-1}
078	ML_LR	lapse rate of air temperature between 850 and 500 hPa.	
079	UL_LR	lapse rate of air temperature between 500 and 200 hPa.	
080	SWEAT	Severe Weather Threat Index after Miller (1972).	-
081	CT	Cross Totals Index. $CT = td_{850} - ta_{500}$, after Miller (1967).	K

Continuation of Table S1			
No.	Variable	Definition	Units
082	SWISS00	$SWISS00 = SHOW + 0.4WSh_{3-6\_mag} + 0.1(ta_{600} - td_{600})$, following Huntrieser et al. (1997). SHOW defined in 056, WSh3_6_mag is wind shear 3-6 km above ground.	-
083	SWISS12	$SWISS12 = LI_{sfc} + 0.1WSh_{0-3\_mag} + 0.1(ta_{650} - td_{650})$, following Huntrieser et al. (1997). LI_sfc is the LI for a near surface parcel defined in 071.	-
084	TEI850	Total Energy Index at 850 hPa, following Darkow (1968).	J kg^{-1}
085	DCI	Deep Convective Index = $(ta_{850} - td_{850} - LI_{sfc})$ after Barlow (1993).	K
086[a]	LPI	Lightning Potential Index, after Frisbie et al. (2009).	-
087	DTE	the difference between the equivalent potential temperature near the surface (2 m) and 300 hPa after Atkins and Wakimoto (1991).	K
088 .. 097	ta_i	air temperature on pressure levels 1000–100 hPa with 100 hPa step.	K
098[a]	x	Longitude	degree
099[a]	y	Latitude	degree
100[a]	doy	day of the year (1-365)	-
101[a]	hod	hour of the day (00, 06, 12, 18 UTC)	-
102[a]	zg_s	surface geopotential	m^2 s^{-2}
End of Table			

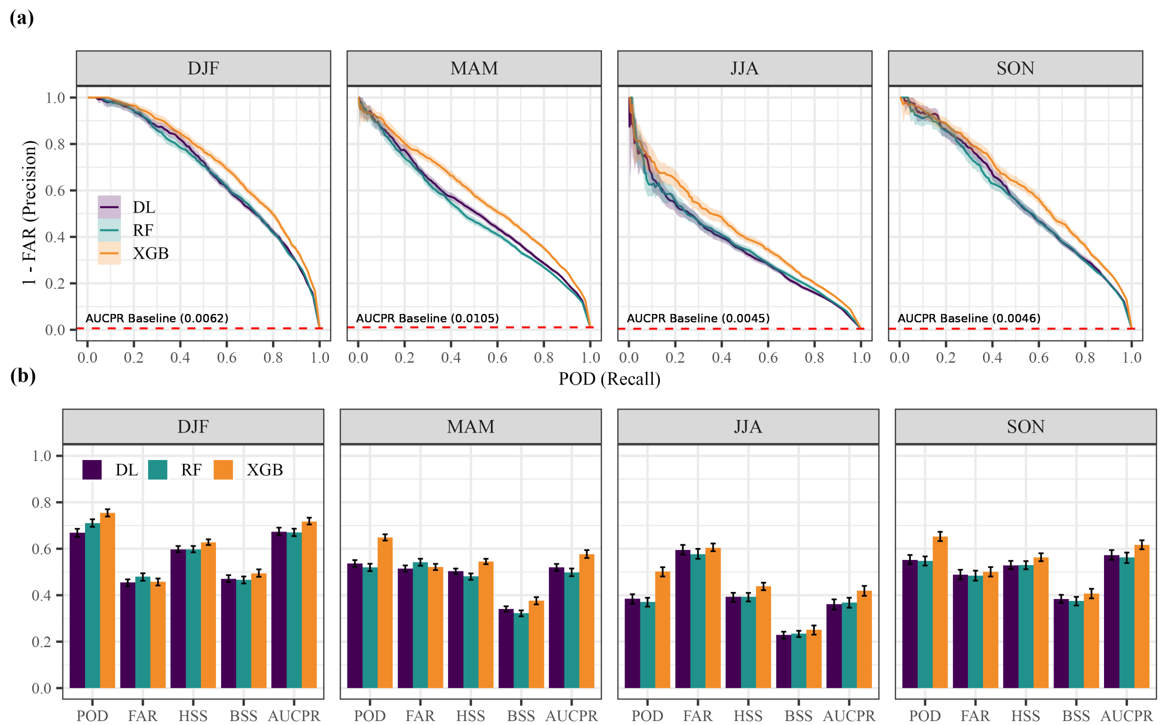

Figure S3. Seasonal (a) precision-recall curves and (b) skill evaluation metrics for DL, RF and XGB. The shaded areas and error bars denote the symmetric 95% confidence interval obtained from 300 bootstrap resamples.

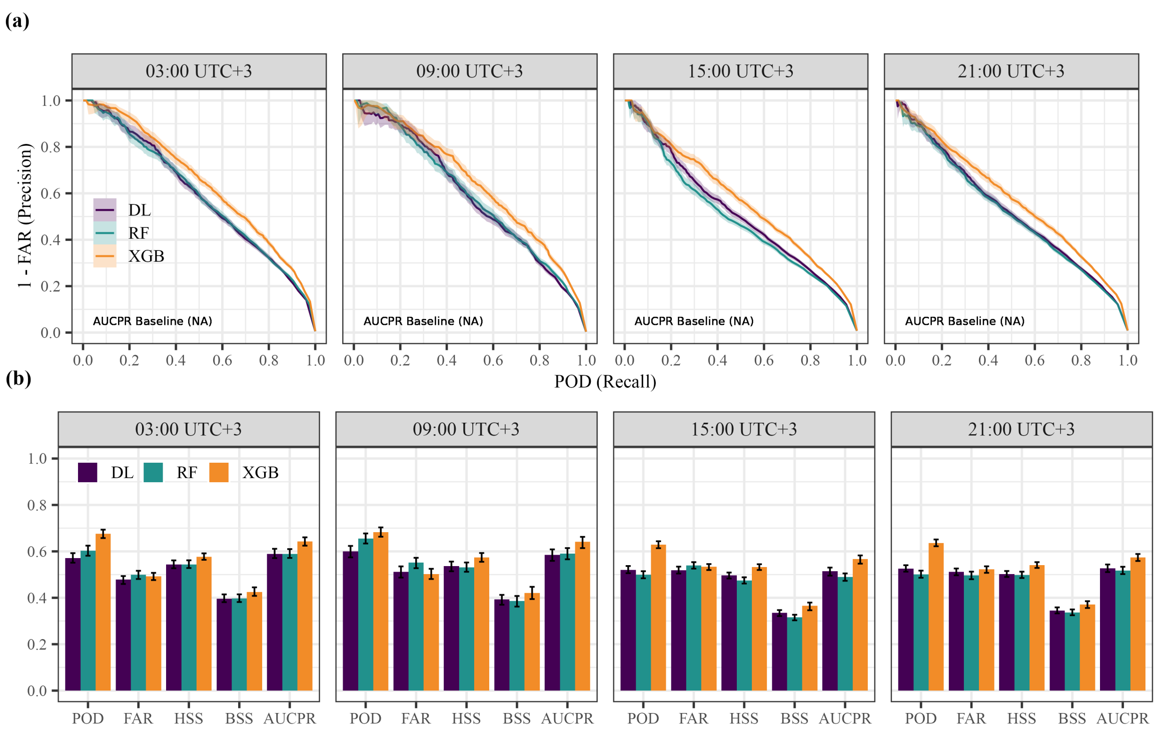

Figure S4. Same as Fig. S3, but from a diurnal perspective.

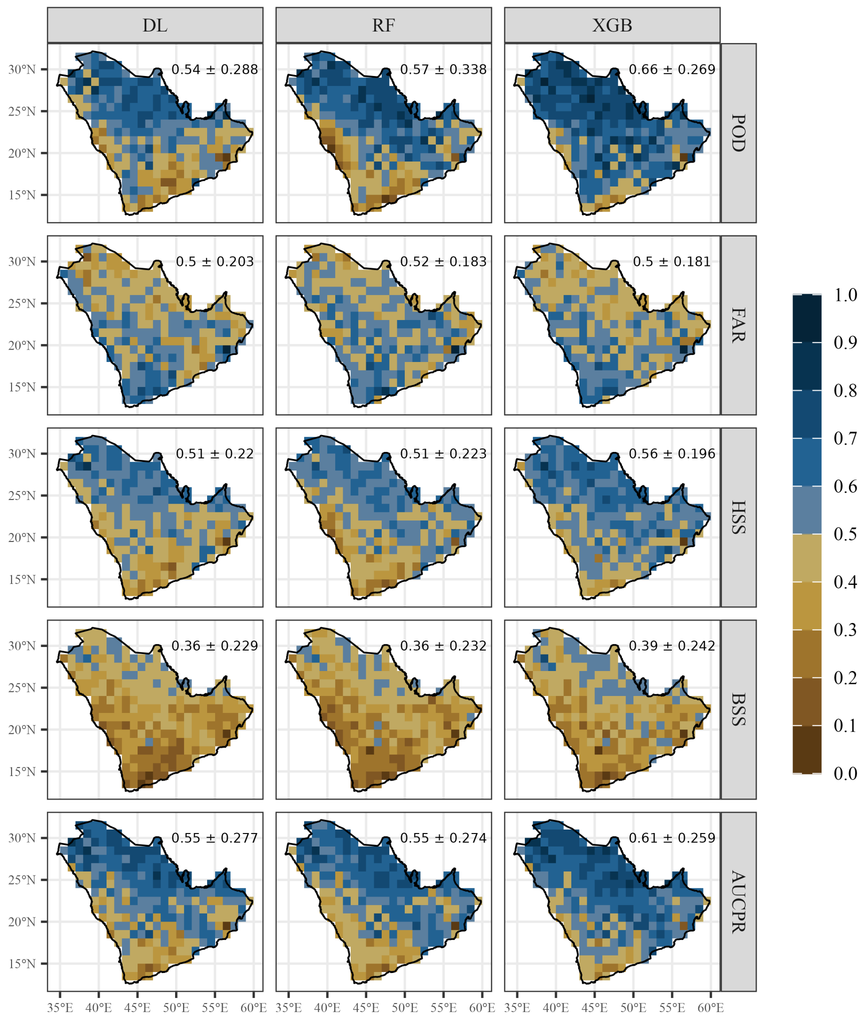

Figure S5. Spatial evaluation metrics for DL, RF, and XGB. The text on top right shows the spatial mean and standard deviation ($\mu \pm 2\sigma$).

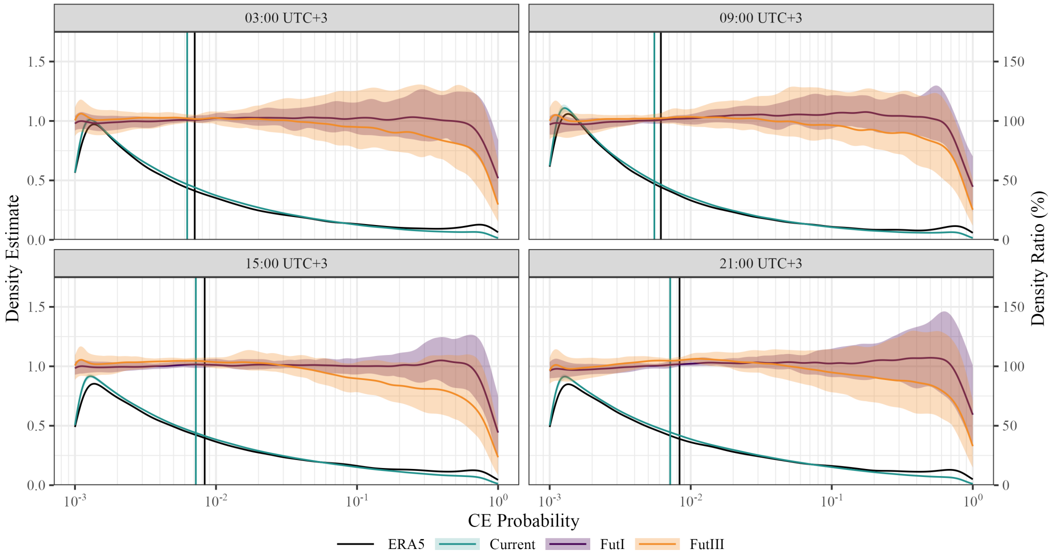

Figure S6. Same as Fig. 3, but from a diurnal perspective.

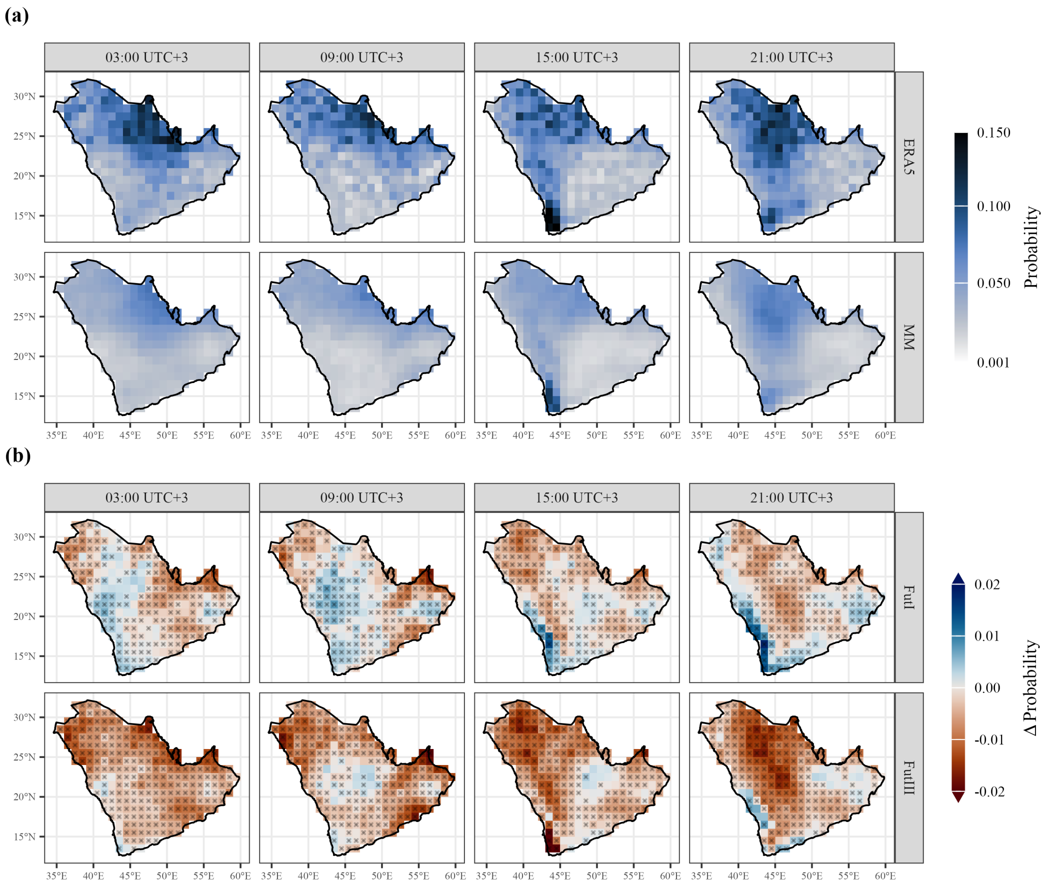

Figure S7. Same as Fig. 4, but from a diurnal perspective.

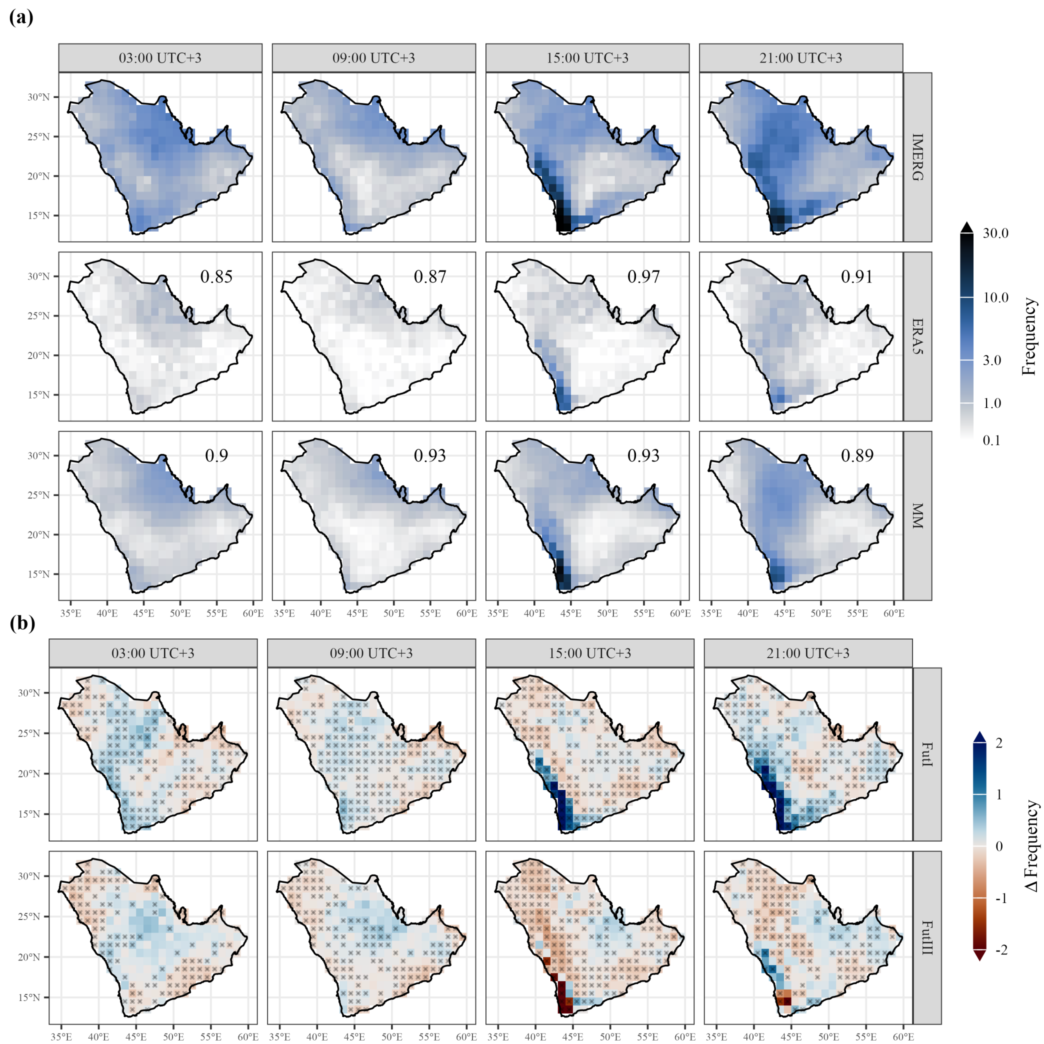

Figure S8. Same as Fig. 5, but from a diurnal perspective.

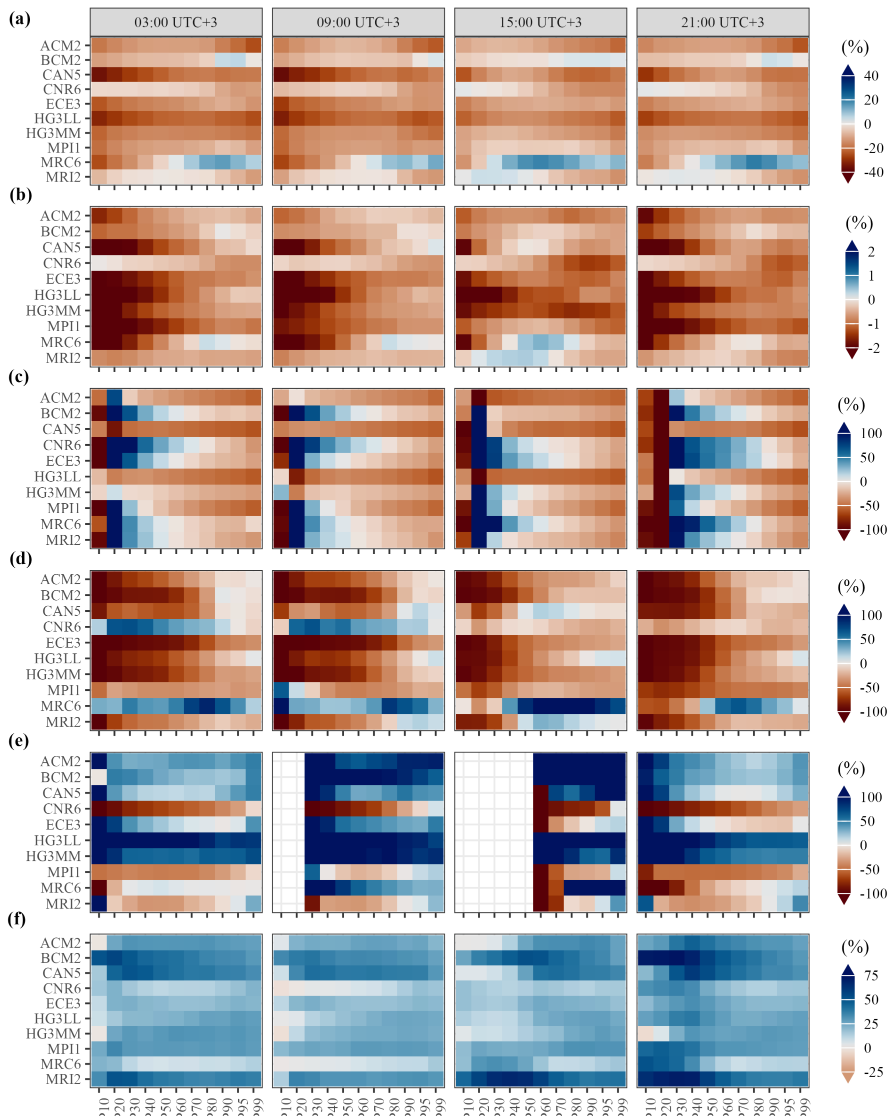

Figure S9. Same as Fig. 7, but from a diurnal perspective.

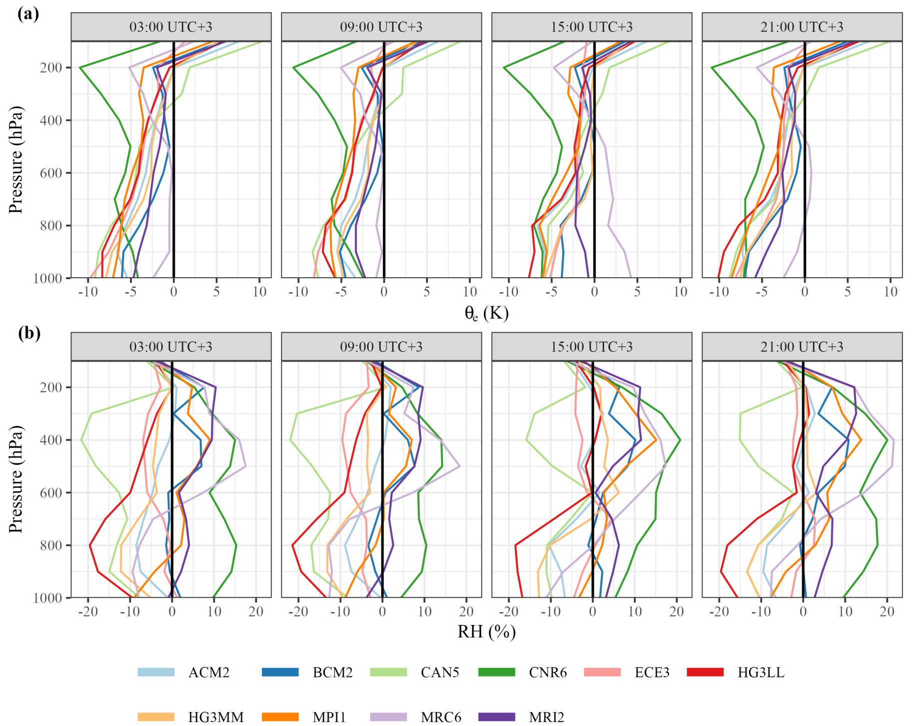

Figure S10. Same as Fig. 8, but from a diurnal perspective.

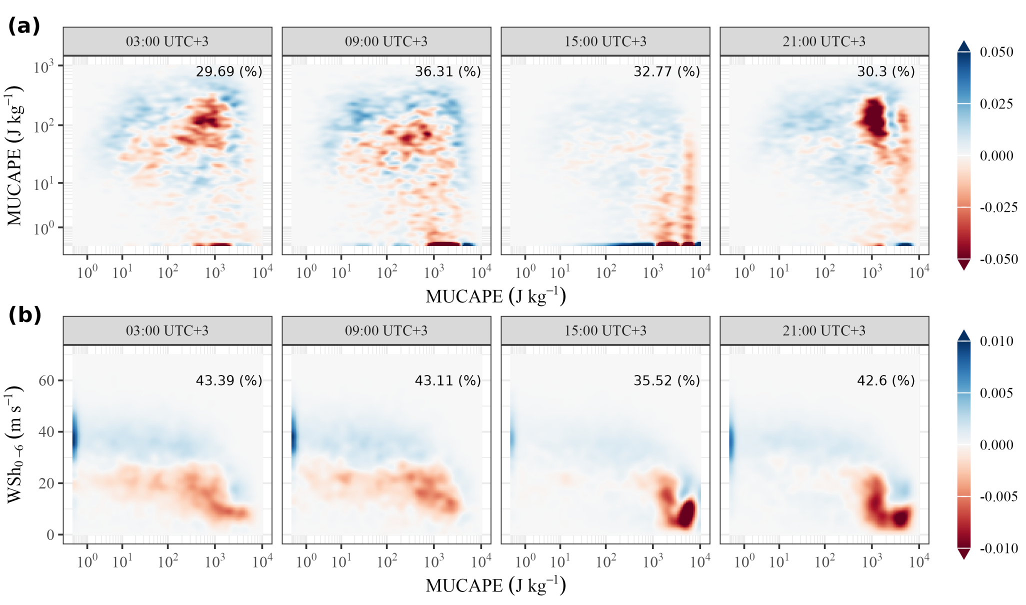

Figure S11. Same as Fig. 9, but from a diurnal perspective.

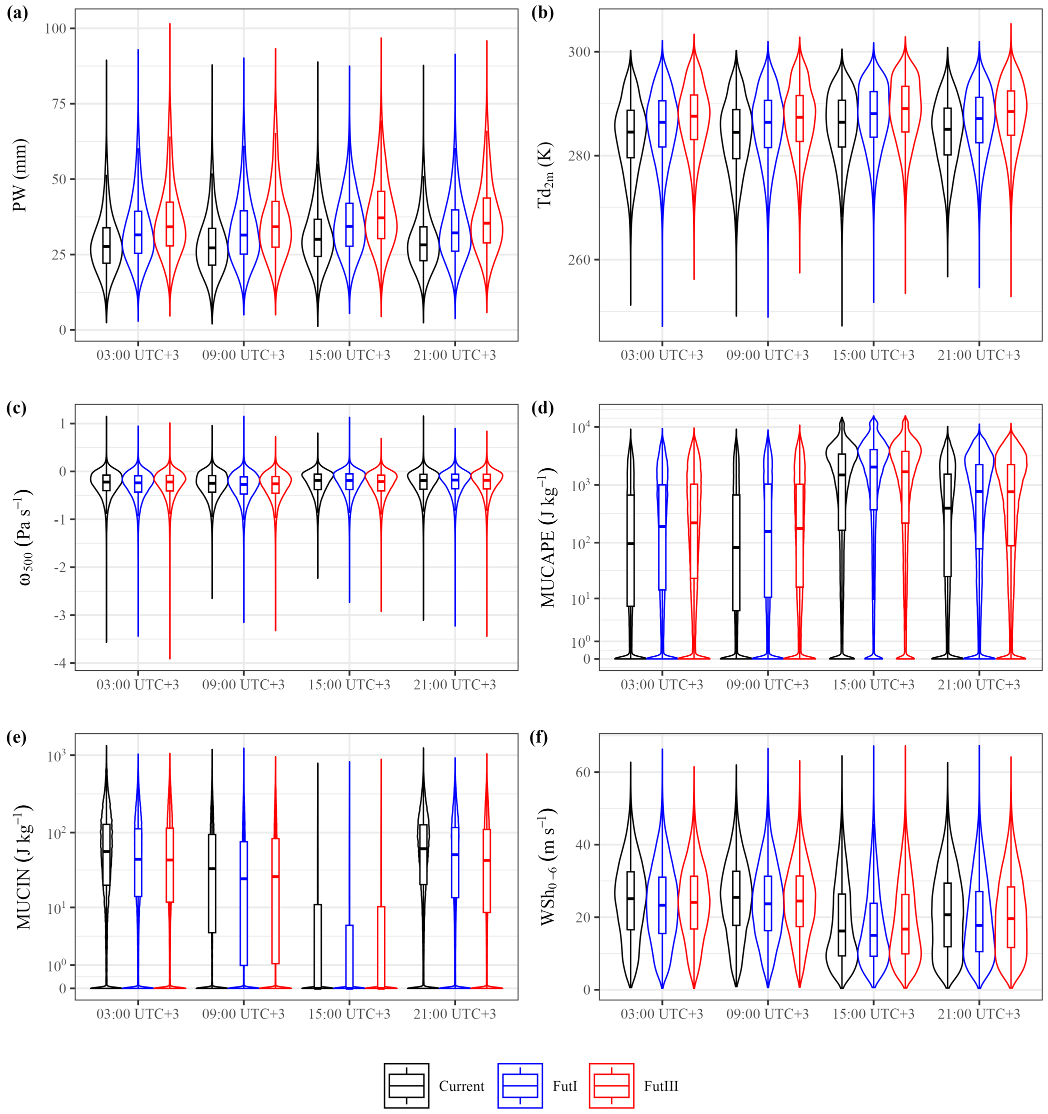

Figure S12. Same as Fig. 10, but from a diurnal perspective.

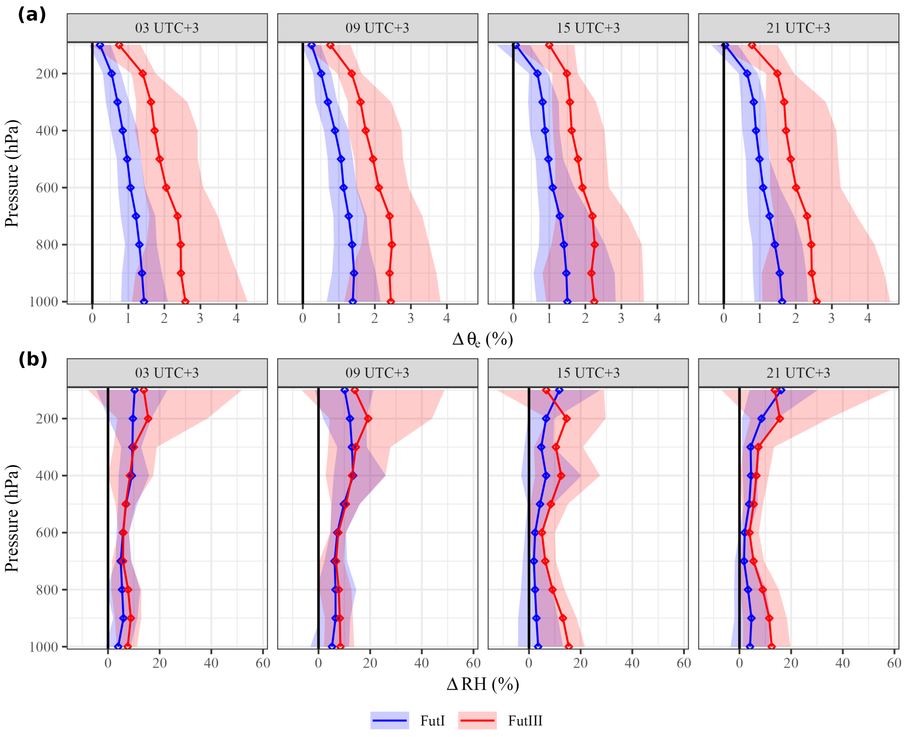

Figure S13. Same as Fig. 11, but from a diurnal perspective.

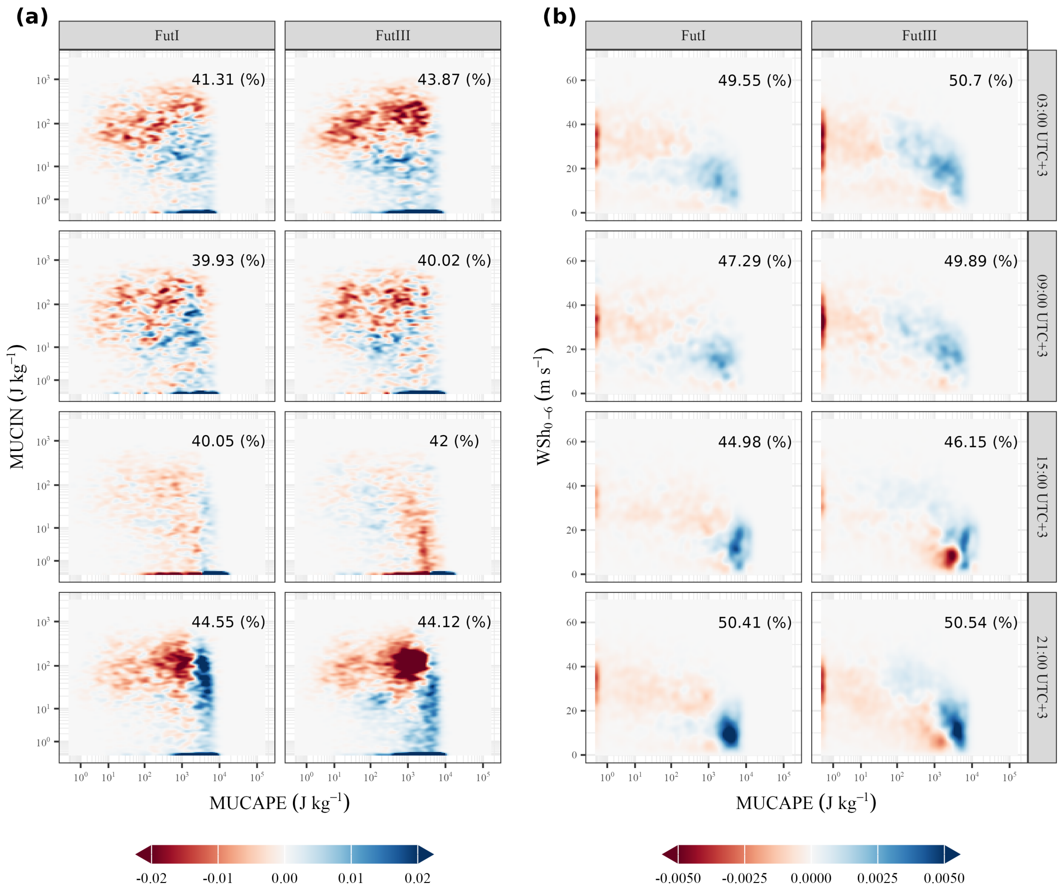

Figure S14. Same as Fig. 12, but from a diurnal perspective.

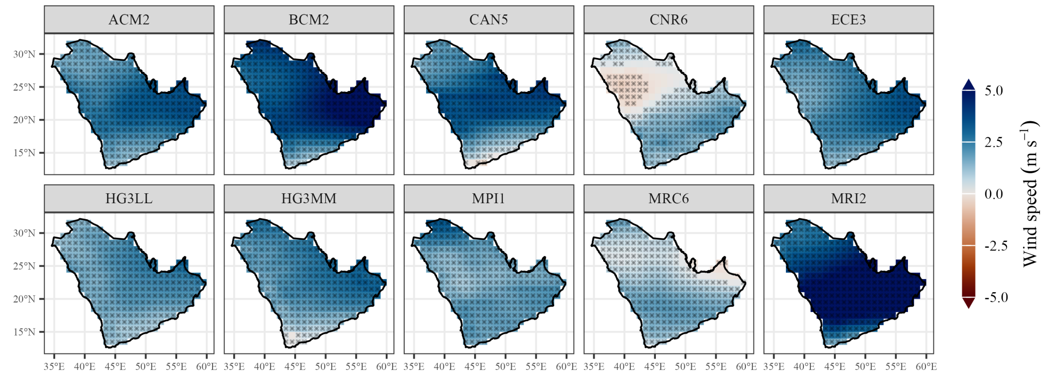

Figure S15. Bias in 700–400 hPa layer-mean wind speed during DJF for CMIP6 models relative to ERA5. Stippling indicates statistical significance at the 95% confidence level based on a two-sided Student's t-test..

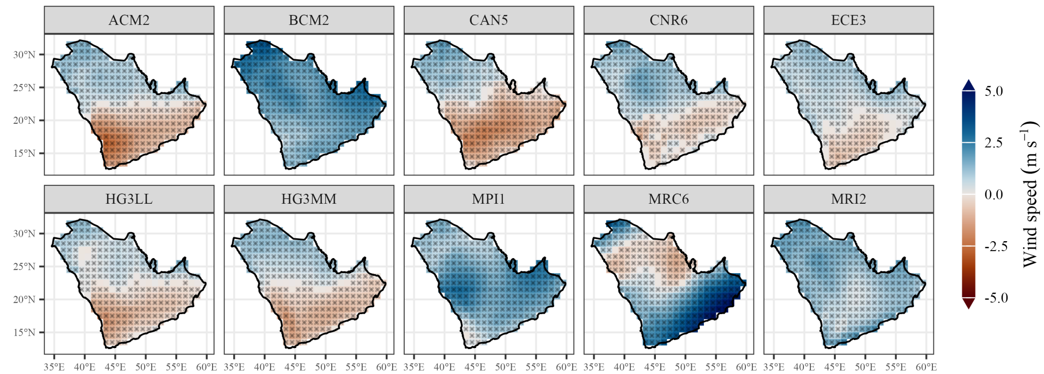

Figure S16. Same as Fig. S15, but for JJA.

Table S2. Global warming levels (°C) from observations[a] and CMIP6 models estimated for the periods shown in Table 2.

Model	Current (+1.22 °C)[b]	*FutI* (+2.22 °C)[b]	*FutIII*(+4.22 °C)[b]
ACM2	1.15	2.35	4.23
BCM2	1.22	2.27	4.23
CAN5	1.23	2.77	4.24
CNR6	1.13	2.24	4.25
ECE3	1.24	2.33	4.27
HG3LL	1.06	2.40	4.23
HG3MM	1.05	2.24	4.29
MPI1	1.23	2.24	4.27
MRC6	1.20	2.23	4.24
MRI2	0.94	2.26	4.24

a The average global warming for the period 2001 - 2024 relative to the pre-industrial level (1850 - 1900) is +1.05°C, based on the area-weighted average of Berkeley Earth, GISTEMP, HadCRUT5, and NOAA Global Temp datasets.

b Regional warming level.

Table S3. Optimal RF Hyperparameters.

Hyperparameter	Value
num.trees	1000
mtry	8
min.node.size	10
sample.fraction	0.9
splitrule	extratrees
replace	false
class.weights	{0: 1, 1: 10}

Table S4. Optimal XGB Hyperparameters.

Hyperparameter	Value
nrounds	1750
eta	0.05
max_depth	12
subsample	0.6
min_child_weight	3.0
min_split_loss	0.0
colsample_bytree	0.6
reg_lambda	10.0
reg_alpha	0.0323
scale_pos_weight	1.0

Table S5. Optimal DL Architecture & Hyperparameters.

Layer	Units	Activation Function	Dropout	Batch Normalization
Input Layer	102	–	–	FALSE
1st Dense Layer	496	LeakyReLU (0.1)[a]	0.25	TRUE
2nd Dense Layer	528	LeakyReLU (0.15)	0.20	TRUE
3rd Dense Layer	96	LeakyReLU (0.12)	0.25	TRUE
Output Layer	1	Sigmoid	–	FALSE
Optimiser: Adam (learning rate: 5E-05)				
Loss: Binary Focal Cross-entropy (gamma=1.0, alpha=0.35)				

[a] Negative Slope

Table S6. Beta Calibration Parameters.

Model	a	b	c
DL	1.6394	1.7540	0.2395
RF	0.9192	1.5436	-4.8831
XGB	0.2706	0.6714	-1.0583

Table S7. Seasonal mean and spread ($\mu \pm 2\sigma$) of CE components from the MM ensemble at the current regional warming level, percentage change at *FutI* and *FutIII* relative to the current climate.

		Mean	Change (%)	
	Season	Current	*FutI*	*FutIII*
PW (mm)	DJF	23.64±04.97	10.40±05.97	25.32±12.03
	MAM	29.41±06.68	11.70±10.03	26.89±13.44
	JJA	38.71±14.90	13.65±11.13	30.47±12.54
	SON	30.96±04.80	11.62±12.79	26.93±19.90
Td_{2m} (K)	DJF	280.34±03.54	00.49±00.51	01.16±00.84
	MAM	284.57±03.80	00.56±00.59	01.19±00.96
	JJA	290.34±04.16	00.50±00.41	01.10±00.47
	SON	286.38±03.53	00.42±00.95	01.03±01.00
ω_{500} ($\mathrm{Pa\,s^{-1}}$)	DJF	-0.31±00.16	06.73±17.17	03.41±25.34
	MAM	-0.27±00.17	02.40±23.22[a]	03.84±30.60[a]
	JJA	-0.13±00.15	16.31±29.46	30.03±45.14
	SON	-0.27±00.15	08.98±22.80	10.75±35.05
MUCAPE ($\mathrm{J\,kg^{-1}}$)	DJF	145.28±171.02	14.49±32.92	69.29±80.48
	MAM	1170.92±1120.19	20.89±40.75	46.10±81.75
	JJA	3254.63±2370.86	09.22±15.56	15.91±31.24
	SON	1213.73±731.73	08.74±56.37[a]	25.93±82.58[a]
MUCIN ($\mathrm{J\,kg^{-1}}$)	DJF	61.85±38.47	-11.44±17.35	-7.86±42.40
	MAM	73.12±64.01	-5.63±32.89	-10.55±30.24
	JJA	54.92±53.93	-22.02±42.70	-32.49±52.62
	SON	47.21±52.35	-6.89±33.63	-6.94±51.64
$WSh_{0\text{-}6}$ ($\mathrm{m\,s^{-1}}$)	DJF	31.61±05.06	-2.25±10.33[a]	-5.09±08.82
	MAM	21.21±04.49	-5.71±15.25	-4.41±20.81
	JJA	11.10±05.23	05.14±17.25	09.31±16.01
	SON	18.42±02.82	-0.12±16.23[a]	00.97±33.02[a]

[a] Models' agreement on the sign of change is less than 70%.

Table S8. Same as Table S7, but from a diurnal perspective.

		Mean	Change (%)	
	Hour	Current	*FutI*	*FutIII*
PW (mm)	03:00 UTC+3	28.95±05.42	14.48±05.00	28.11±14.44
	09:00 UTC+3	28.50±05.01	15.98±06.85	29.61±14.41
	15:00 UTC+3	31.13±05.63	12.68±04.02	26.02±10.28
	21:00 UTC+3	29.48±05.48	14.02±04.04	28.34±16.48
Td_{2m} (K)	03:00 UTC+3	284.12±02.54	00.62±00.43	01.13±00.72
	09:00 UTC+3	283.99±02.53	00.64±00.51	01.10±00.61
	15:00 UTC+3	285.80±02.90	00.59±00.47	01.07±00.55
	21:00 UTC+3	284.57±02.62	00.67±00.41	01.19±00.88
ω_{500} ($\mathrm{Pa\,s^{-1}}$)	03:00 UTC+3	-0.27±00.16	05.69±15.46	06.32±21.22 [a]
	09:00 UTC+3	-0.29±00.15	09.14±17.78	11.13±21.31
	15:00 UTC+3	-0.24±00.14	-3.46±16.66	11.61±24.77
	21:00 UTC+3	-0.24±00.14	-5.26±13.63	03.12±31.60 [a]
MUCAPE ($\mathrm{J\,kg^{-1}}$)	03:00 UTC+3	591.49±444.55	29.98±40.99	44.49±72.12
	09:00 UTC+3	641.90±478.90	23.59±38.27	38.29±75.61
	15:00 UTC+3	2212.93±2004.17	17.93±25.74	14.44±38.25
	21:00 UTC+3	1043.63±674.10	34.75±42.14	41.29±73.68
MUCIN ($\mathrm{J\,kg^{-1}}$)	03:00 UTC+3	95.77±69.74	-15.56±23.03	-24.49±21.61
	09:00 UTC+3	68.18±47.13	-17.85±32.18	-20.04±26.51
	15:00 UTC+3	18.85±18.46	-21.43±39.37	-9.53±40.53
	21:00 UTC+3	91.84±70.75	-9.96±14.78	-24.95±25.79
WSh_{0-6} ($\mathrm{m\,s^{-1}}$)	03:00 UTC+3	24.60±04.04	-4.66±13.52	-2.28±13.82[a]
	09:00 UTC+3	25.09±04.11	-4.18±13.65	-2.48±13.06[a]
	15:00 UTC+3	18.53±03.26	-5.38±12.77	02.65±19.76[a]
	21:00 UTC+3	21.23±03.46	-7.65±12.73	-1.40±21.35[a]

[a] Models' agreement on the sign of change is less than 70%.

References

Atkins, N. T. and Wakimoto, R. M.: Wet Microburst Activity over the Southeastern United States: Implications for Forecasting, Weather and Forecasting, 6, 470–482, https://doi.org/10.1175/1520-0434(1991)006<0470:WMAOTS>2.0.CO;2, 1991.

Barlow, W. R.: A New Index for the Prediction of Deep Convection, in: Preprints, 17th Conference on Severe Local Storms, pp. 129–132, American Meteorological Society, St. Louis, MO, 1993.

Darkow, G. L.: The Total Energy Environment of Severe Storms, Journal of Applied Meteorology and Climatology, 7, 199–205, https://doi.org/10.1175/1520-0450(1968)007<0199:TTEEOS>2.0.CO;2, 1968.

Frisbie, P. R., Colton, J. D., Pringle, J. R., Daniels, J. A., Ramey, Jr., J. D., and Meyers, M. P.: Lightning Prediction by WFO Grand Junction using Model Data and Graphical Forecast Editor Smart Tools, in: Preprints, Fourth Conference on the Meteorological Applications of Lightning Data (89th AMS Annual Meeting), American Meteorological Society, https://ams.confex.com/ams/89annual/techprogram/paper_149101.htm, 2009.

Haklander, A. J. and Van Delden, A.: Thunderstorm Predictors and Their Forecast Skill for the Netherlands, Atmospheric Research, 67–68, 273–299, https://doi.org/10.1016/S0169-8095(03)00056-5, 2003.

Huntrieser, H., Schiesser, H. H., Schmid, W., and Waldvogel, A.: Comparison of Traditional and Newly Developed Thunderstorm Indices for Switzerland, Weather and Forecasting, 12, 108–125, https://doi.org/10.1175/1520-0434(1997)012<0108:COTAND>2.0.CO;2, 1997.

Miller, R. C.: Notes on Analysis and Severe-Storm Forecasting Procedures of Military Weather Warning Center, Tech. Rep. 200, Air Weather Service (MAC), United States Air Force, 1967.

Miller, R. C.: Notes on Analysis and Severe-Storm Forecasting Procedures of the Air Force Global Weather Central, Tech. Rep. 200 (Rev.), Air Weather Service (MAC), United States Air Force, Scott Air Force Base, IL, 1972.

Murphy, A. H.: A New Vector Partition of the Probability Score, Journal of Applied Meteorology and Climatology, 12, 595–600, https://doi.org/10.1175/1520-0450(1973)012<0595:ANVPOT>2.0.CO;2, 1973.

Naeini, M. P., Cooper, G., and Hauskrecht, M.: Obtaining Well Calibrated Probabilities Using Bayesian Binning, Proceedings of the AAAI Conference on Artificial Intelligence, 29, https://doi.org/10.1609/aaai.v29i1.9602, 2015.

Reymann, M., Piasecki, J., Hosein, F., Larabee, S., Williams, G., Jimenez, M., and Chapdelaine, D.: Meteorological Techniques, Technical Note AFWA/TN-98/002, Air Force Weather Agency (AFWA), Offutt AFB, IL, https://www.weather.gov/media/zhu/ZHU_Training_Page/Met_Tutorials/Meteorological_Techniques.pdf, approved for public release; distribution is unlimited. Update to Air Weather Service Manual 105-56 “Forecasting Techniques.” UNCLASSIFIED., 1998.